Spatiotemporal dynamics of cellulose during enzymatic hydrolysis studied by infrared spectromicroscopy

Journal:	*Green Chemistry*
Manuscript ID	GC-ART-08-2023-003279.R2
Article Type:	Paper
Date Submitted by the Author:	05-Nov-2023
Complete List of Authors:	Jeoh, Tina; University of California Davis, Bio. and Ag. Engineering Nill, Jennifer; University of California Davis; Amyris Biotechnologies Inc Zhao, Wujun; Lawrence Berkeley National Laboratory; Genus plc Narayanasamy, Sankar Raju; Lawrence Berkeley National Laboratory; Lawrence Livermore National Laboratory Chen, Liang; Lawrence Berkeley National Laboratory; TikTok Holman, Hoi-Ying; Lawrence Berkeley National Laboratory

1 **Spatiotemporal dynamics of cellulose during enzymatic hydrolysis**
2 **studied by infrared spectromicroscopy**
3

4 Tina Jeoh[1,*], Jennifer Danger Nill[1,2,§], Wujun Zhao[3,4,§], Sankar Raju Narayanasamy[3,5,§], Liang Chen[3,6],
5 and Hoi-Ying N. Holman[3,*]

6 [§] These authors contributed equally to this manuscript

7 [1]Biological and Agricultural Engineering, University of California Davis, Davis, CA

8 [2]Current: Amyris, Emeryville, CA

9 [3]Berkeley Synchrotron Infrared Structure Biology (BSISB), Lawrence Berkeley National Lab (LBNL),
10 Berkeley, CA

11 [4]Current: Genus PLC, DeForest, Wisconsin

12 [5]Current: Biosciences and Biotechnology Division, Physical and Life Science, Lawrence Livermore
13 National Laboratory, Livermore, CA

14 [6]Current: TikTok, Mountain View, California

15

16 [*]Corresponding Authors

Abstract

18 Cellulose, a sustainable source of fermentable glucose and nanomaterials, exists as highly-ordered,
19 solvent-inaccessible fibrils held by intra- and intermolecular hydrogen bonds. Cellulose hydrolysis rates
20 and extents are limited by the availability and accessibility of productive cellulase binding sites at the
21 water-cellulose interface. There is a need to understand how spatial heterogeneity of celluloses impact
22 hydrolysis kinetics. We report a real-time, in situ infrared spectromicroscopy study of enzymatic cellulose
23 hydrolysis in buffer with micrometer-scale spatial mapping. Algal cellulose depletion by a purified
24 cellobiohydrolase Cel7A was tracked as time-resolved decreases in the absorption peak intensities of the
25 glycosidic bond (1161 cm^{-1}), C2-O2 (1112 cm^{-1}), C3-O3 (1059 cm^{-1}), and C6-O6 rotamers (1034 cm^{-1},
26 1013 cm^{-1}, and 997 cm^{-1}). Depletion kinetics varied spatially, with peak intensities decreasing to zero in
27 some areas and plateauing in others. Hydration impacted cellulose ordering where C6-O6 and C3-O3
28 peaks were sharp, narrow, and centered at higher frequencies when hydrated, but broader, less well-
29 defined and centered at lower frequencies when dried. Temporal trends of the Lateral Order Index (LOI),
30 Total Crystallinity Index (TCI), and Hydrogen Bonding Index (HBI) indicated that hydrolysis by Cel7A
31 preferentially removed less extensively hydrogen bonded cellulose, without significantly affecting the
32 overall crystallinity of highly ordered cellulose.

1 Introduction

34 The circular bioeconomy—wherein renewable feedstocks are sustainably utilized to offset energy and
35 valuable materials conventionally produced with petroleum—is key to achieving worldwide carbon
36 neutrality (1,2). Cellulose from lignocellulosic biomass is the most abundant biopolymer on the planet
37 that can be a renewable, sustainable feedstock for fuels and chemical production. On the one hand,
38 complete depolymerization of cellulose yields soluble glucose that can be fermented into biofuels or
39 biochemicals. On the other hand, cellulose can be processed into nanofibrils and nanocrystals with

40   superior mechanical properties for use with advanced biomaterials (3–5). Environmentally sustainable
41   and tunable processes to achieve saccharification and/or nanomaterial production are best achieved by
42   enzyme-mediated reactions (6–8). However, controlling enzyme catalyzed reaction kinetics has long been
43   a challenge. Cellulose hydrolysis is characterized by rapidly declining reaction rates despite the remaining
44   abundance of cellulose in the reaction, which has been postulated to be limited by the accessibility of
45   cellulose to cellulases (9–20). The interaction of cellulase enzymes with cellulose is an interfacial reaction
46   on structurally heterogeneous fibrils (13,18,21). An understanding of spatial and temporally resolved
47   changes of cellulose structural properties during enzyme hydrolysis reaction is needed for controlling
48   bulk reaction kinetics.

49   Advances in in-situ, spatial and time-resolved analytical methods have provided insights into cellulase-
50   cellulose and cellulase-lignocellulosic biomass interactions. For example, atomic force microscopy
51   (AFM) has advanced knowledge in microstructural changes in cellulose and the dynamics of cellulytic
52   enzymes at cellulose interfaces (21–23); super-resolution single molecule imaging by total internal
53   reflectance fluorescence (TIRF) microscopy revealed interaction dynamics of cellulases at cellulose
54   interfaces, quantifying enzyme off-rates and processivities (24,25); coherent Raman spectroscopy
55   contributed to understanding of the role of plant cell wall architecture in limiting enzyme accessibility to
56   cellulose (26). However, an unaddressed knowledge gap hindering full understanding of the mechanism
57   of enzymatic cellulose and lignocellulose hydrolysis is the role of cellulose supramolecular structure in
58   limiting productive cellulase interactions.

59   Fourier transform infrared (FTIR) spectromicroscopy is one of the most sensitive, label-free, physical
60   techniques for studying spatially resolved changes in biomolecular structure and composition (27). FTIR
61   has been used to characterize cellulose crystallinity, crystalline morphology and intrafibril hydrogen
62   bonding attributed to enzymatic action; however, these studies have primarily been on dried, post-treated,
63   bulk cellulosic samples subjected to varying sample preparation and measurement environment (e.g.
64   surface tension, concentration, humidity, temperature) (14,28–32). In one example, Corgie et al. reported
65   evidence of decrystallization and preference for Iα or Iβ crystalline morphology by *Thermobifida fusca*
66   Cel5A, Cel6B and Cel9A cellulases (28); but a follow-up study of the same reactions using different
67   sample preparation methods by Kruer-Zerhusen et al. reported no conclusive impact of the enzyme action
68   on cellulose crystallinity (29). One strategy to circumvent such artifacts is by in situ, time- and spatial-
69   resolved FTIR spectromicroscopy of cellulose undergoing enzymatic hydrolysis. However, the need for
70   buffered reactions is a barrier to FTIR measurements because of strong mid-IR absorption by water.
71   Closed microfluidics have been used to conduct in situ FTIR spectromicroscopy of enzymatic treatment
72   of plant biomass for bioenergy production (27,33–35). In this study, we used a novel open microfluidic
73   device that enabled us to meet the need for on-demand access to the sample and the need for sustainable
74   detection of FTIR spectral signals from the infrared hydride-OH region and the molecular fingerprint
75   region.

76   This work was motivated by the hypothesis that local molecular ordering of cellulose can limit the
77   accessibility of these so-called 'productive binding sites' where cellulase can successfully form
78   complexes for hydrolysis, and that spatial variability in cellulose influences and is influenced by cellulase
79   hydrolysis. Here, we present the first real-time, micrometer-scale, spatially resolved investigation of
80   cellulose undergoing enzymatic hydrolysis by Synchrotron radiation-based FTIR (SR-FTIR)
81   spectromicroscopy. Using a broadband, high-brightness synchrotron infrared source instead of the
82   conventional thermal source enabled wavelength-dependent diffraction-limited spatial resolution with
83   ~200 times increase in signal-to-noise ratio. This superior resolution allows for identification of changes
84   in structures within crystalline cellulose in space and in time, which is unavailable using a Globar source.

85   Using well characterized, highly crystalline cellulose fibrils from the green algae *Cladophora*
86   *aegagropila*, we demonstrated the impact of hydration on molecular ordering in cellulose fibrils by noting
87   changes in the vibration bands of C2-O, C3-O, and C6-O of cellulose that participate in intra- and
88   intermolecular hydrogen bonding. Spatial and temporal heterogeneity in changes in cellulose abundance
89   and molecular order during hydrolysis by a purified *Trichoderma reesei* Cel7A (Cel7A) at 37°C in buffer
90   were recorded and analyzed.

91   ## 2   Experimental

92   **2.1   Preparation of cellulose and cellulase**
93   Algal cellulose fibrils were isolated from the green algae *Cladophora aegagropila* as described
94   previously (18). Briefly, marimo balls (Plants for Pets, Amazon, LLC) were pulled apart and rinsed with
95   tap water to remove excess sand before subjecting to alternating alkali (1 M sodium hydroxide, 4°C) and
96   bleach (0.3 % sodium hypochlorite, 100 mM sodium acetate, pH 5, 70°C) treatments to isolate pure
97   cellulose. Cellulose fibrils were washed extensively then stored at 4°C in nanopure water with 0.02%
98   sodium azide. Algal cellulose fibrils were previously characterized to be ~ 90% crystalline, ~70%
99   cellulose Iα, with a reducing end content of ~ 4 μmoles/g (18), and a productive Cel7A binding capacity
100   of ~ 2 μmoles/g (10,13). *Trichoderma reesei* Cel7A (*Tr*Cel7A) was purified from Celluclast 1.5L (Sigma
101   C2730) and stored in 5 mM sodium acetate, pH 5 as previously described (21).

102   **2.2   Real-time synchrotron radiation (SR)-FTIR monitoring of cellulose in buffered systems**

103   ### 2.2.1 *Controlling sample hydration environment in open microfluidics*
104   The microfabricated open-channel microfluidics membrane device shown in Figure 1A is a stack of three
105   structures (Figure 1B) with a silicone sample-support plate (Structure 2, Figure 1.B) fixed between two
106   layers of polydimethylsiloxane (PDMS) microchannel structures. A 3 mm x 3 mm silicon nitride (SiNx)
107   porous membrane with a thickness of 300 μm and a pore diameter of 500 nm (SiMPore Inc.) was coated
108   with 100 nm of gold via a sputtering system (AJA International) after being inserted into the opening of the
109   silicone plate. The pore size is small enough that the coated-membrane surface reflects IR illumination
110   uniformly without any noticeable scattering (34), PDMS microchannel in the upper humidity control plate
111   (Structure 1) and in the bottom buffer reservoir plate (Structure 3) were fabricated using standard soft
112   lithography technique. SU-8 3010 (Kayaku Advanced Materials) was spin-coated onto a silicon wafer.
113   Sylgard 184 silicone elastomer kit (Dow) was cast onto the master mold with a 10:1 ratio of elastomer and
114   curing agent followed by curing at 80 °C for 3 h. The microchannels were 20 μm wide and its thickness
115   was measured to be 10 μm by a profilometer (Veeco Instruments) (Figure 1.C). The bottom structures
116   (Structure 3, Figure 1.B) were for producing a passive vertical imbibition of buffer solution from the
117   microchannel below through the porous membrane to the sample on the membrane surface. The top layer
118   (Structure 1) is a humidity-control microfluidic structure with four microchannel arrays to provide a
119   horizontal flow of moisture that blankets the sample chamber to minimize evaporation or condensation on
120   the porous membrane during the experiment (Figure 1.C). A vertical through-square was carved out using
121   a craft cutter system (Silhouette America), followed by plasma bonding to the top microchannel. The
122   plasma treatment forms a sealed two-channel fluid system with individually accessible top and bottom
123   microchannel. Silicon-based PSA tape was used as an intermediate layer to create PDMS-silicone sheet
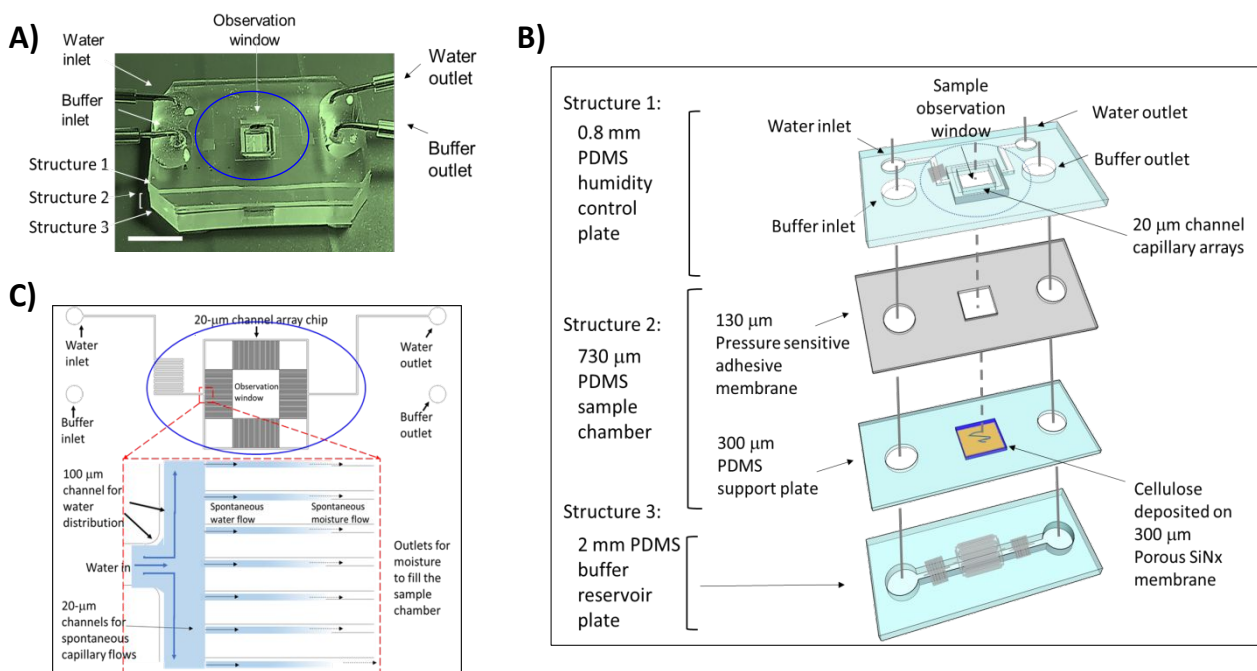124   constructs.

125

Figure 1: Method for controlling relative humidity (RH) and imbibition flow of thin liquid film in an open-channel microfluidics membrane device for real-time synchrotron FTIR imaging of cellulose ordering and composition during hydrolysis in situ. A) A photograph of the three-structure stacked PDMS microfluidic membrane device. Scale bar =5 mm. B) A schematic showing construction of the open-channel microfluidics membrane device consisting of the top humidity control microchannel plate and the middle sample support plate and the nanopore SiNx membrane sealed by a pressure sensitive polymer layer. The two stacked structure and the bottom buffer reservoir plate were sealed by plasma treatment. (C) An exploded schematic view of the micro-channel capillary arrays controlling the RH in the sample chamber. Arrows show the directions of the water and moisture flows.

126

2.2.2   SR-FTIR of cellulose changes during dehydration

127

128   Samples for recording SR-FTIR spectra of cellulose at varying states of hydration were prepared by
129   depositing three 20 µL aliquots of algal cellulose (0.025mg/mL) fibrils onto the SiNx porous membrane
130   with a diameter of 0.5 µm (SiMPore Inc., New York, USA) in the open-channel microfluidics membrane
131   device (36,37). Cellulose fibrils were settled under ambient conditions for 40 minutes before raising the
132   temperature to 37 °C. Excess liquid was removed by wicking. Time-series FTIR spectra were collected
133   every ~ 10-11 seconds over ~37 minutes (200 points) as the sample dehydrated through evaporation. The
134   recorded relative humidity by the humidity sensor (HiLetgo 2pcs Si7021 GY-21 Industrial High Precision
135   Temperature Humidity Sensor with I2C IIC interface for Arduino Low Power CMOS IC Module, Amazon)
136   was 24%. SR-FTIR spectral measurements were conducted as described below.

2.2.2   SR-FTIR of cellulose undergoing enzymatic hydrolysis

137

138   Experimental samples for monitoring cellulose hydrolysis by SR-FTIR were prepared by depositing and
139   air-drying 60 µL of algal cellulose (0.025mg/mL) fibrils onto the SiNx membrane in the open-channel
140   microfluidics membrane device, followed by an infiltration of 20 µL of Cel7A (0.5 µmole/g) through the
141   cellulose (Step1, Figure 2). The enzyme and substrate were equilibrated in air at ambient conditions (~20

142   ^{o}C) for ~ 40 minutes at room temperature, then mounted onto the FTIR microscope for optical alignment
143   and location of regions of interest (ROI) (Step 2, Figure 2). The experiment was initiated by using a
144   syringe pump (Harvard 33 DD Twin Syringe Pump Infuse/Withdraw) to infuse 1 mM sodium acetate
145   buffer at 0.3 µL/min into the fluid distribution channel connected to the bottom microchannel (Step 3,
146   Figure 2), and a temperature controller (Cole Parmer 12107 20 Digital Polystat) to raise the temperature
147   of the FTIR microscope stage to 37°C (Step 4, Figure 2). The acetate solution wicked upwards by
148   capillary forces through the SiNx pores maintained a buffered reaction at the membrane surface. At 37 ^{o}C
149   the system maintained a relative humidity of ~80%. With the initiation of reaction, infrared absorption
150   measurements were collected and monitored to evaluate the quality of the experiment in real-time,
151   followed by detailed post-experiment analysis (Step 5, Figure 2).

152   ### *2.2.3   SR-FTIR spectral measurements*

153   All SR-FTIR measurements were made at the infrared beamline at the Advanced Light Source (ALS)
154   (Lawrence Berkeley National Laboratory, CA, USA) using a Nicolet Magna 760 FTIR spectrometer
155   equipped with a liquid nitrogen cooled Mercury Cadmium Telluride (MCT) detector, and an all-reflective
156   optics infrared microscope (Nicolet Nic-Plan, Thermo Scientific, Inc., MA, USA). Mid-infrared photons
157   emitted from the synchrotron, which are linearly polarized in the plane of the orbit and circularly
158   polarized above and below the storage ring plane, were focused with a numerical aperture (NA = 0.65)
159   objective through the cellulose fibrils onto the gold-coated membrane surface inside the open-channel
160   microfluidics membrane device, and reflection SR-FTIR measurements by the transflection mode over a
161   mid-infrared wavenumber range of 4000 – 650 cm^{-1} were made over time. Each real-time spectrum
162   represents an average of 32 scans at a spectral resolution of 4 cm^{-1} with an absorption peak position
163   accuracy of 0.01 cm^{-1}.

164   To image the spatiotemporal dynamics of cellulose during enzymatic hydrolysis, we typically divided the
165   entire view-field of the cellulose fibrils into equal-sized 5×5-µm squares before raster scanning, collecting
166   full SR-FTIR spectra at each pixel. Time-elapsed mapping of sample areas were conducted using in-
167   house software written in the Python programming language (version 3.6). The master program controlled
168   the movement of the microscope stage, spectra collection of FTIR spectrometer and data storage in the
169   OMNIC software program (version 9.8, Thermo Fisher Scientific, Inc.) using the Dynamic Data
170   Exchange (DDE) protocol. The source code of our python programs for controlling the microscope and
171   FTIR bench is available upon request. Raw spectral data reported in this study is available for download
172   (38).

173   ### *2.2.4   SR-FTIR data processing and analysis*

174   Data were processed using the OMNIC 8.3 software (Thermo Fisher Scientific, Inc.). Raw spectra were
175   converted from reflectance to absorbance and subjected to baseline correction and noise-reduction. The
176   corrected spectra were transformed to second derivative spectra (7-point Savitsky-Golay smoothing
177   polynomial order 3), and the transformed spectra were inverted and analyzed without normalization. The
178   position of the peak of the inverted 2nd derivative spectrum was used to resolve overlapping peaks and
179   the intensity was used to estimate relative abundances through the Beer-Lambert Law.

180

181
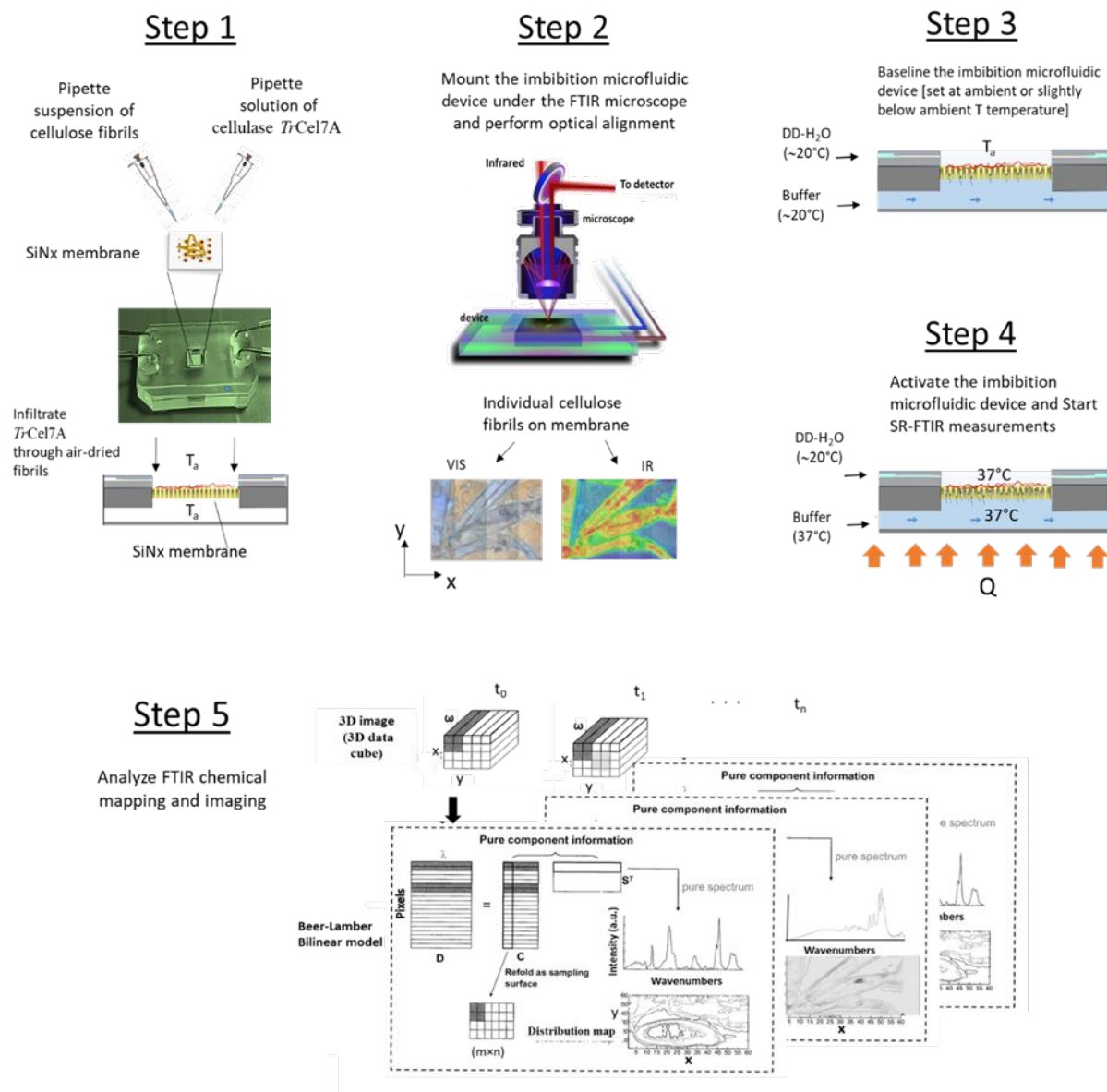
Figure 2: Experimental and data analytic procedure for continuous monitoring of cellulose hydrolysis by
Cel7A by SR-FTIR in the open-channel microfluidics membrane device.

3   Results

3.1   Time-resolved SR-FTIR spectra of cellulose in varying hydration states

FTIR spectra of cellulose in the literature are primarily of dried cellulose; thus, the assignment of the
peaks unique to cellulose are of dry cellulose. Since our experiments are with hydrated cellulose in buffer,
we examined the impact of hydration on the signature peaks of cellulose. Time-resolved spectra of wet
cellulose undergoing evaporative drying were recorded over the course of $\sim$ 37 minutes (Figure 3).
Cellulose remained fully hydrated for about the first $\sim$6 minutes, after which a sharp drop in the
absorption amplitudes of the water peaks at 1650 cm^{-1} (H-O-H bending mode) and 2150 cm^{-1} (H-O-H
vibration mode), respectively, were observed (Figure 3B). A second sharp drop in the amplitude of the
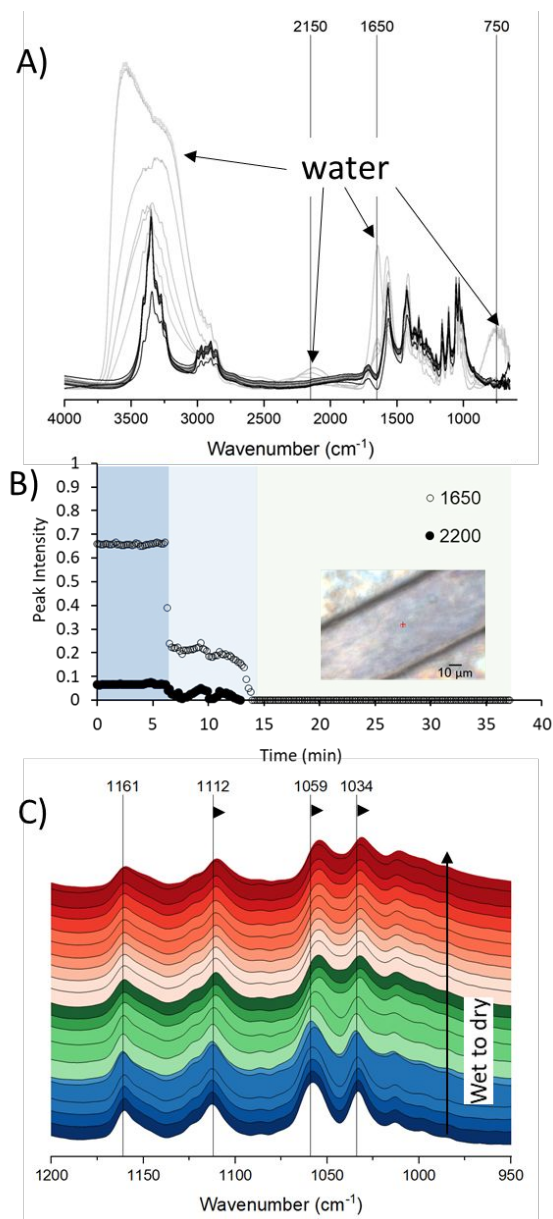1650 and 2150 cm^{-1} peaks to zero at about 15 minutes further indicated full removal of moisture.

Figure 3: A) Time-resolved SR-FTIR spectra of cellulose undergoing evaporative dehydration at 25% RH at 37°C. Absorption peaks at ~ 3000 – 3700 cm^{-1}, 2150 cm^{-1}, 1650 cm^{-1} and 750 cm^{-1} associated with water molecules are indicated. Lighter to darker grayscale gradient indicate progression from hydrated to dry spectra. B) Intensities of the 1650 and 2150 cm^{-1} absorption bands of water over the course of the experiment. Inset shows brightfield image of the location on the cellulose fibril where the spectra were recorded. C) A closer view of the spectra between 950 – 1200 cm^{-1} showing shifts to lower frequencies (arrows) by the vC2-O2 (1112 cm^{-1}), vC3-O3 (1059 cm^{-1}) and the primary vC6-O6 (1034 cm^{-1}) peaks due to drying. Color-coding indicate fully hydrated spectra in blue, spectra during drying in green, and spectra after drying in red. Spectra recorded every ~ 2 min are shown.

194　　Strong absorption of mid-IR energy by water can be an impediment to successful FTIR imaging of
195　　biological reactions in situ. Strong water absorption peaks centered around 2150 cm^{-1}, 1650 cm^{-1}, and 750
196　　cm^{-1} wavenumbers obscure less prominent absorbance signals from other constituents in these regions.

7

197   Moreover, water molecules can form hydrogen bonds with neighboring molecules with a spectrum of
198   different bond lengths and stretching vibrational frequencies, resulting in the OH functional groups of
199   water forming continuous vibrational frequencies and giving an extensively broad and dominant infrared
200   absorption in the hydrogen bonding (X-H) 3000 – 3700 cm^{-1} region (39,40) (light gray spectra in Figure
201   3A). The absorption due to water, however, generally avoids the fingerprint region (~900 – 1400 cm^{-1})
202   where vibration peaks of the C-O bonds of cellulose dominate. Under controlled hydration levels, the
203   presence of absorbed water at 1650 cm^{-1} and the absorption peaks in the fingerprint region of cellulose
204   can be clearly distinguished (Figure 3A).

205   ### 3.1.1   *Hydration impacts surface ordering of cellulose*

206   A close look at C-O vibration peaks of cellulose in the fingerprint region reveal subtle but clear impact of
207   moisture. The absorption peak centers of C2-O2 (~1112 cm^{-1}), C3-O3 (1059 cm^{-1}), and C6-O6 (primary at
208   1034 cm^{-1}, secondary at 1013 cm^{-1}, and minor at 997 cm^{-1}) shifted from higher to lower frequency when
209   dried (Figure 3C, Table 1). In cellulose, the hydroxyl groups of C2, C3 and C6 participate extensively in
210   intra- and intermolecular hydrogen bonding (41,42) (Figure 4). The shift towards lower frequency upon
211   drying suggests weaker C-O bonds in the absence of moisture; conversely, that water imposes rigidity to
212   these bonds. The intensities of the O-C1-O, C2-O2 and C3-O3 absorption peaks see a moderate decrease
213   of ~20 % upon drying (Table 1, Supplementary Material 2). The synchrotron infrared light is polarized;
214   thus, these changes suggest dehydration induced changes in the orientation of the C1-O-C4 glycosidic
215   bonds and C2-O2 and C3-O3 bonds in the cellulose fibrils such that their orientations become less
216   parallel to the linearly polarized synchrotron light. The absorption bands of these functional groups in
217   cellulose molecules are known to be more intense when their orientations are in parallel with polarized
218   light (43–48).

219

220   *Table 1: Cellulose peak positions and intensities in the fingerprint region in dry or hydrated states. Peak*
221   *intensities and positions tracked over time are given in Supplementary Materials 2. Peak assignments for*
222   *all cellulose-associated peaks are given in Supplementary Materials 1, Table S1.1.*

Cellulose peaks in the fingerprint region	Wavenumber at Peak Center (cm^{-1})[1]		Peak Shift when dried	Peak Intensity (A.U.)[1]		Intensity change when dried
	Dry	Hydrated		Dry	Hydrated	
ν_{AS} O-C1-O	1161 ± 0.2	1161 ± 0.3	No change	0.19 ± 0.0023	0.22 ± 0.0052	- 17%
ν_{S} O-C1-O	1207 ± 0.3	1207 ± 0.3	No change	0.04 ± 0.0010	0.04 ± 0.0018	No change
νC1-O1	1152 ± 1.6	1152 ± 0.3	No change	0.11 ± 0.011	0.11 ± 0.0052	No change
νC2-O2	1111 ± 0.4	1113 ± 0.3	- 2.2 cm^{-1}	0.21 ± 0.0027	0.25 ± 0.0045	- 16%
	1123 ± 0.3	1124 ± 0.2	- 0.4 cm^{-1}	0.08 ± 0.0026	0.1 ± 0.0033	- 19%
νC3-O3	1057 ± 1.0	1059 ± 0.9	- 2.5 cm^{-1}	0.31 ± 0.011	0.38 ± 0.013	- 22%
Minor νC6-O6 (*gt*)	997 ± 0.8	998 ± 0.7	- 0.7 cm^{-1}	0.15 ± 0.0042	0.06 ± 0.0035	+ 46%

Secondary νC6-O6 (*gg*)	1012 ± 0.5	1013 ± 0.3	- 0.8 cm^{-1}	0.22 ± 0.0026 (1.5:1)*	0.12 ± 0.0034 (2:1)*	+ 60%
Primary νC6-O6 (*tg*)	1032 ± 0.6	1034 ± 0.7	- 1.4 cm^{-1}	0.34 ± 0.0040 (2:1)**	0.34 ± 0.0064 (6:1)**	No change

223　[1]Averaged over the 0 – 5 minutes and 25 – 35 min for dry and hydrated states as shown in Supplementary
224　Materials SM2
225　*Ratio of secondary to minor C6-O6 peak intensities
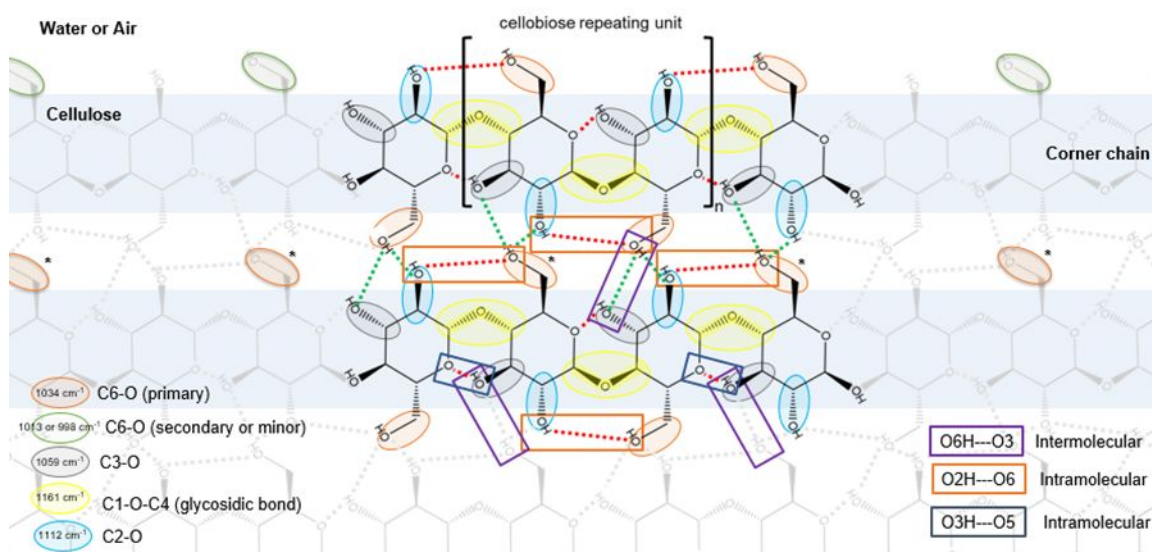226　**Ratio of primary to minor C6-O6 peak intensities
227

Figure 4: Illustration of top down view of the hydrophobic face of cellulose, highlighting C-O bonds and hydrogen bonds characteristic of cellulose I. Red dotted lines indicate intramolecular hydrogen bonds; Green dotted lines indicate intermolecular hydrogen bonds. The C6-O bond can occupy secondary or minor rotamers at cellulose/air interface but likely occupies the primary rotamer within the cellulose structure. C6-O6 bonds in the primary rotameric forms would likely covert to secondary or minor rotamers when exposed to the interface, e.g. if the corner chain is hydrolyzed by Cel7A (indicated by asterisks).

228　Interestingly, the ratios of the average peak intensities of the primary, secondary, and minor absorption
229　bands of C6-O6 shift from ~6:2:1 in the hydrated state to ~2:1.5:1 in the dry state (Table 1, and
230　Supplemental Material 2). Yet, to our knowledge, peak intensities of C6-O6 bonds are not known to
231　change with the orientation of polarized light. The change in intensity ratio is driven by the increase in the
232　intensities of the 1013 cm^{-1} (secondary) and 997 cm^{-1} peaks (minor) when dried, while the intensity of the
233　1034 cm^{-1} peak (primary) remained unchanged. In crystalline cellulose I, *trans-gauche* (*tg*) rotamers of
234　C6-O6 dominate within the crystalline structure, facilitating both the C6-O6$\cdots$HO2 intramolecular
235　hydrogen bond across the glycosidic bond, and the C6-O6H$\cdots$O3 intermolecular hydrogen bond with
236　neighboring cellulose (41,42,49) (Figure 4). Thus, negligible impact of dehydration on the intensity
237　suggests that the primary C6-O6 bonds are not solvent accessible and likely correspond to *tg* rotamers.
238　Intensity increases in the secondary and minor C6-O6 peaks due to dehydration suggest that these are

239   solvent accessible C6-O6 bonds, likely *gauche-gauche* (*gg*) and *gauche-trans* (*gt*) rotamers, respectively
240   (50,51).

241   The absorption peaks associated with the anomeric carbon, both as part of the glycosidic bond (1161 and
242   1207 cm^{-1}) and as free reducing end (1152 cm^{-1}) were minimally impacted by moisture (Figure 3C, Table
243   1, and Supplemental Material 2). The absorption peak centers did not shift from a wet to dry state, and
244   only a slight decrease in intensity (17%) was observed at 1161 cm^{-1} upon drying. It is no surprise that the
245   stiffness of the glycosidic bonds in cellulose I, braced by intramolecular hydrogen bonds (C3O3H···O5
246   and C2O2···HO6) on either side, is not influenced by water. The C1-O1 bond of the free reducing-end,
247   already absorbing at a lower frequency (i.e. less stiff than the glycosidic bond), was also not influenced by
248   water.

249   In general, the impact of moisture appears to be stiffening of the C-O bonds of cellulose involved in intra-
250   and intermolecular hydrogen bonds. At the cellulose/air interface, C2-O6H, C3-O3H and C6-O6H are less
251   likely to engage in hydrogen bonds (intrafibril or with water) than at the cellulose/water interface.
252   Cellulose has been shown to exhibit lower crystallinity indices (CI) in a dry state than in a hydrated state
253   with similar explanations on the role of water in imposing surface ordering (Park et al., 2009). The impact
254   of moisture on C-O vibration peaks of cellulose are summarized in Table 1. The full set of peak
255   assignments for the hydrated IR spectra of cellulose in the 900 – 3500 cm^{-1}, and further discussion on the
256   impacts of hydration/dehydration are provided in Supplementary Material 1 and 2.

257   **3.2   Time- and spatial-resolved SR-FTIR spectra of cellulose undergoing enzyme hydrolysis**
258   IR spectral evolution of algal cellulose undergoing hydrolysis by a purified Cel7A in pH 5 buffer at 37°C
259   was recorded in an 8 x 8 grid every ~9.5 minutes over 15-hours. The imaged region consisted of a thick
260   deposition of cellulose in the bottom half and a sparser deposition of fibrils in the top half (Figure 5).
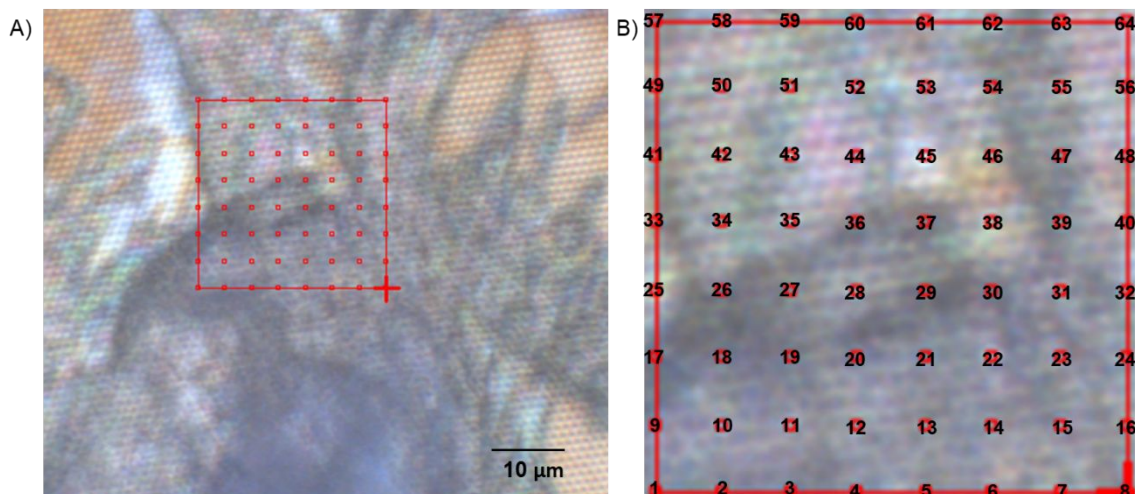

Figure 5: A) Brightfield image of the algal cellulose region examined in this study. IR spectra were recorded at 64 locations every ~ 10 min in an 8x8 grid as shown. B) The imaged area is enlarged, showing the numbering of the locations where spectra were recorded.

261   The characteristic cellulose peaks in the fingerprint region, particularly centered around 1161 cm^{-1}
262   (glycosidic bond), 1112 cm^{-1} (C2-O2), 1059 cm^{-1} (C3-O3), and 1034cm^{-1} (C6-O6) are clearly
263   distinguishable in the time-resolved spectra throughout the reaction (Figure 6B). During the 15-hour
264   reaction, ~ 3 μm water film was maintained for the first ~ 5 hours, after which the water film thickness

265   increased to ~ 12 μm (Supplementary Information 3). The time courses of the intensities of cellulose-
266   associated peaks in the fingerprint region (998, 1013, 1034, 1059, 1112, 1124, 1150, 1161, and 1205 cm^{-1})
267   confirmed negligible interference of water levels on peak intensities in the mapped region (Figure 6B
268   and Supplemental Information 4). Thus, the full time course data could be used to assess changes to
269   cellulose due to enzyme action. Unfortunately, increased water film thickness at > 5 h obscured peaks in
270   the 2700 – 3900 cm^{-1} range hydride-OH region (Figure 6C and Supplemental Information 4).

271   Characteristic amide I and amide II peaks of the enzyme (~1650 cm^{-1} and 1550 cm^{-1}, respectively) were
272   clearly visible at low water levels, but replaced by a strong adsorbed water peak at ~1650 cm^{-1} in the
273   presence of excess water (Figure 6B). A large fraction of enzymes on the surface was most likely washed
274   away; moreover, the dominance of the adsorbed water signal at 1650 cm^{-1} obscured signal from any
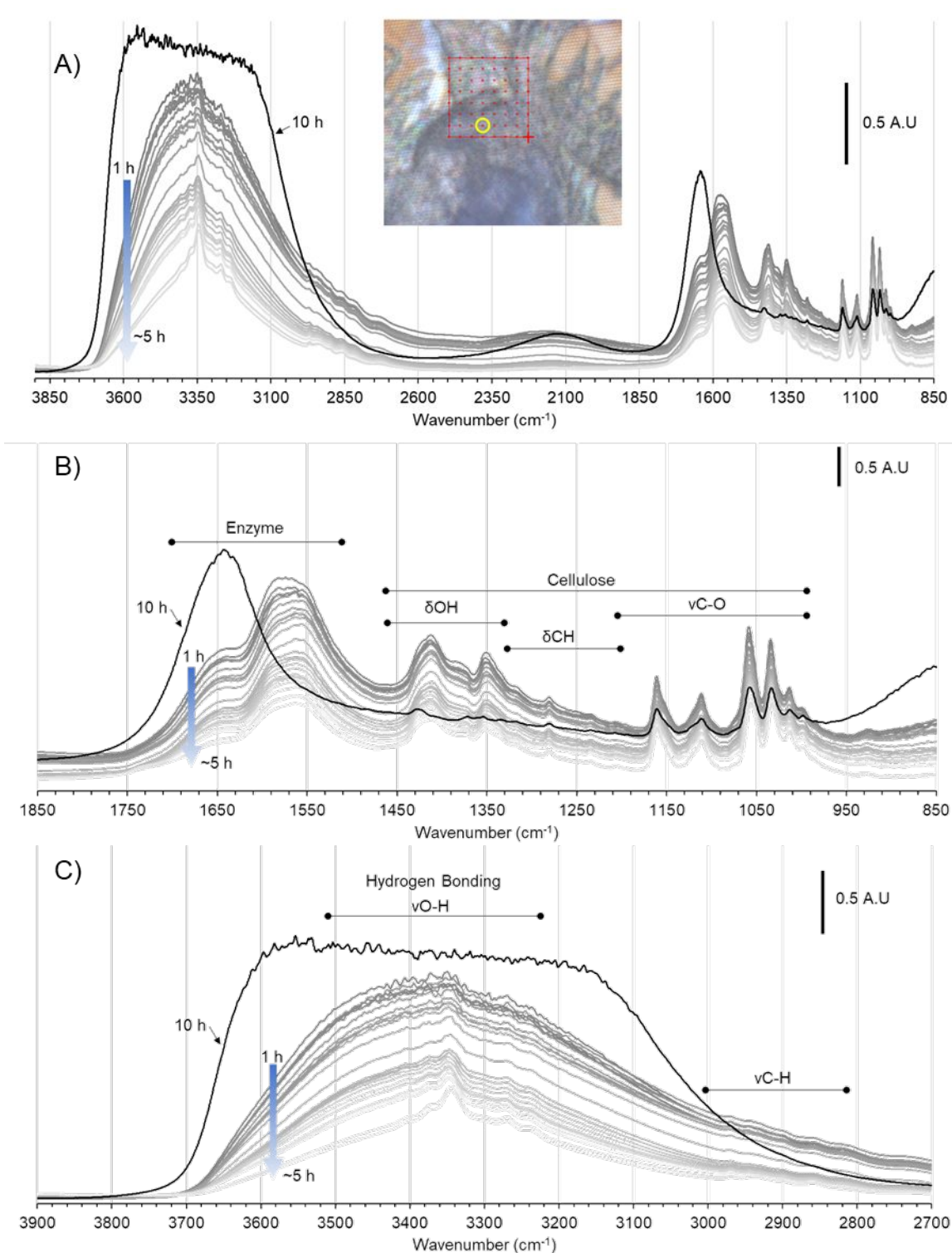275   enzymes that remained bound to cellulose.

Figure 6: A) Full range IR spectra of cellulose undergoing enzymatic hydrolysis collected over 0 – 5 h and at 10 h from the circled location in the inset brightfield sample image. Expansions of the B) 850 – 1850 cm⁻¹ range showing characteristic peaks of cellulose and adsorbed enzymes, and the C) 2700 – 3900 cm⁻¹ range showing C-H vibration and the hydrogen bonding regions of cellulose. The full set of peak assignments for the hydrated IR spectra of cellulose in the 900 – 3500 cm⁻¹ are provided in Table S.1 in Supporting Information.

276

277 ### 3.2.1   *Cellulose depletion by enzymatic hydrolysis*

278 The distribution of cellulose in the imaged region can be visualized as a heat map of the amplitude of the
279 –O-C1-O1- glycosidic bond peak of cellulose at ~1161 cm^{-1} (0 h in Figure 7A). The 0-h heat map,
280 overlaid onto the brightfield image of the observed region, show high intensities (red) mapped to areas
281 with the thicker deposition of cellulose and decreased intensities radiated outwards where cellulose was
282 more thinly distributed (Figure 7B). Time-resolved spatial maps of the intensity of the glycosidic bond
283 peak (~1161 cm^{-1}) show overall depletion of cellulose due to hydrolysis, with heterogeneous rates of
284 depletion in the imaged region (Figure 7A). Over time, there was an overall decrease in the ~1161 cm^{-1}
285 peak amplitude, with an apparent shrinking of the cellulose 'particle'. The amplitude of the ~1161 cm^{-1}
286 peak decreased faster near the particle edges (Figure 7C), in accordance with previous observations of a
287 surface erosion mechanism (20,53). Within 4 hours, signal from the ~1161 cm^{-1} peak was confined in the
288 bottom left quadrant of the imaged region. The peak intensities of cellulose νC-O peaks in the fingerprint
289 region (1034, 1059, and 1112 cm^{-1}) generally tracked that of the 1161 cm^{-1} glycosidic bond peak (Figure
290 7B).

291 Based on the temporal trends of the cellulose peak intensities, the imaged area can be grouped into four
292 regions (i, ii, iii, and iv in Figure 7C). The cellulose peak intensities in region i do not decrease to zero
293 suggesting incomplete cellulose hydrolysis during the 15 hours; furthermore, some points within the
294 region exhibit increased peak intensities in the first 0 – 5 hours. Cellulose peak intensities in region ii
295 decreased throughout the 15 hours. Cellulose peaks in region iii similarly decreased over the course of
296 hydrolysis, with peak intensities decreasing to below detection (reaching zero intensity) within the 15
297 hours, indicating complete hydrolysis of cellulose in this region. The rates of intensity decrease in regions
298 ii and iii reflected trends reminiscent of typical cellulose hydrolysis kinetics with an initial rapid decrease
299 followed by significantly slower rates of depletion. Region iv, where cellulose was sparser, had low
300 intensities, noisier data, and show a baseline shift with increased water into the sample at ~ 5 hours. Thus,
301 region iv will not be discussed further.

302
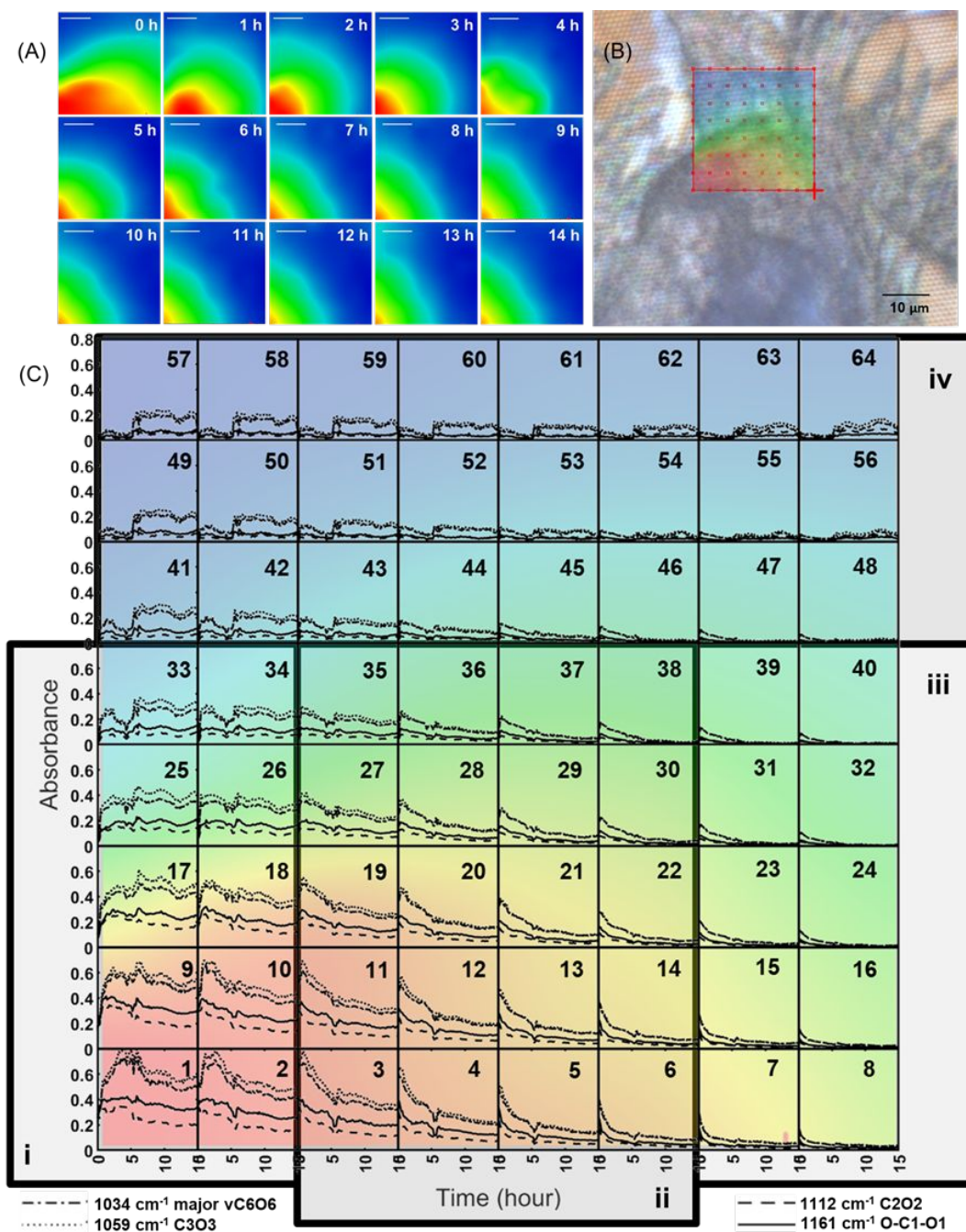
303

Figure 7: A) Heat map of the evolution of the peak intensity of the glycosidic bond peak at ~1161 cm⁻¹ over 15 hours in the imaged region in Figure 5B. Highest peak amplitudes are mapped as red, with decreasing amplitudes from orange to yellow to green to blue. B) The 0-h heat map from (A) overlaid on the imaged region. C) Time course of the amplitudes of the cellulose vibration bands of C6-O6 at 1034 cm⁻¹, C3-O3 at ~1059 cm⁻¹, C2-O2 at ~1112 cm⁻¹ and O-C1-O glycosidic bond at ~1161 cm⁻¹. Plots are arranged in 8x8 grid corresponding to locations in Figure 5B where spectra were recorded. The x-axes are time in hours (0 to 15 hours); y-axes are absorbances/peak intensities (0 – 0.8). The 0-h heat map from (A) is overlaid to show relative intensities of the 1161 cm⁻¹ peak at the start of the time course.

304   *3.2.2   Hydration impact on molecular ordering in region i*

305   The intensities of C3-O3 (1059 cm^{-1}) and primary C6-O6 (1034 cm^{-1}) vibration peaks in region i
306   exhibited unusual increasing trends within the first 1-5 hours not due to changes in the amount of
307   cellulose at these locations (Figure 7C). A closer examination of the spectra reveals broad C3-O3 and C6-
308   O6 peaks composed of multiple populations at point 1, 9 and 17 within the first hour (Figure 8). With
309   increasing time, the C3-O3 and C6-O6 peaks narrowed, sharpened and increased in intensity with
310   improved separation of the two peaks. These trends indicate initial disorder in cellulose where the C3-O3
311   and C6-O6 bonds occupy several conformations that become more ordered with time. In crystalline
312   cellulose I, C3-O3H and C6-O6H engage in both intra- and intermolecular hydrogen bonding as both
313   hydrogen acceptor and donor (41,42) (Figure 4), and their fixed locations would manifest as narrow,
314   sharp peaks in the IR spectra as was seen in the hydrated cellulose spectra (Figure 3C). Disordering of the
315   cellulose molecules that disrupt or distort hydrogen bonds manifest as multiple populations of C3-O3H
316   and C6-O6H, thus broadening and shifting of the C3-O3 and C6-O6 peaks (54,55) as seen in the dry
317   cellulose spectra (Figure 3C). The experiment was initiated by the addition of buffer to an air-dried
318   sample. Thus, one explanation for this observed increase in molecular ordering of cellulose in region i is
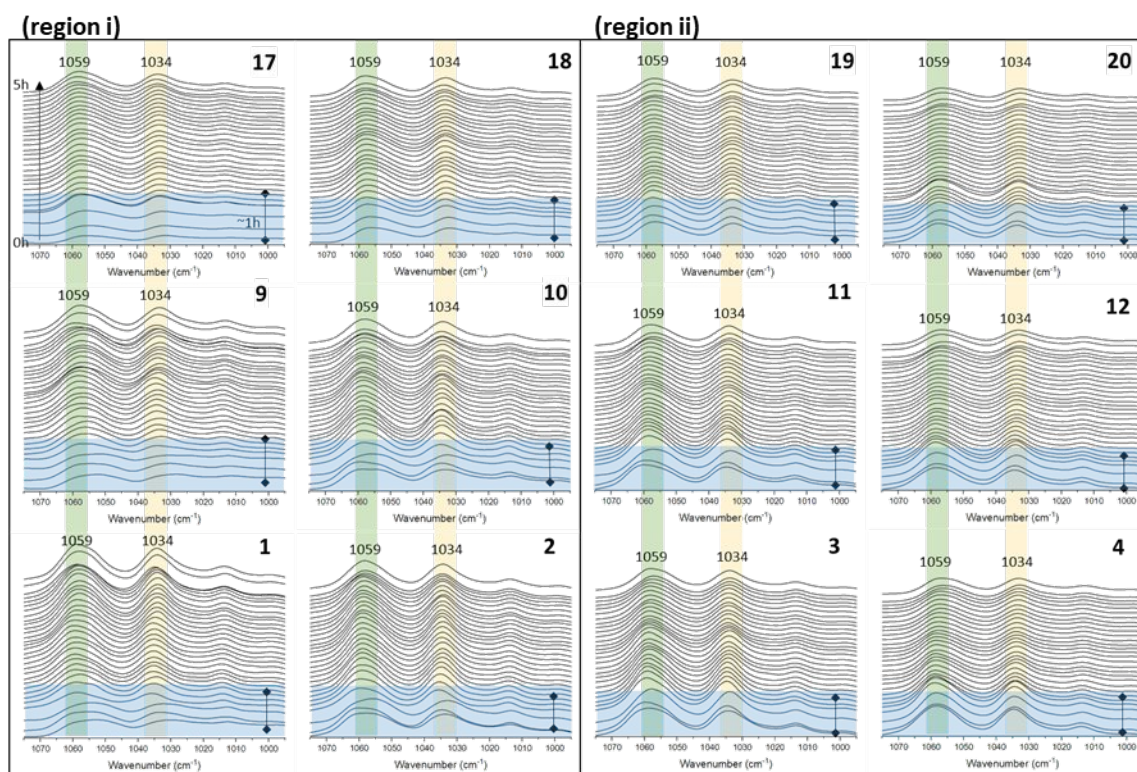319   slower initial hydration of the notably thicker deposition of cellulose.

*Figure 8: FTIR spectra recorded every ~9.5 min over the course of 5 hours in the range of 950 –
1075 cm^{-1} corresponding to locations within regions i and ii. Plot numbers (1-4, 9-12, and 17-20)
correspond to locations shown in Figure 5B and 7C. The spectra are arranged in increasing time
order from bottom to top as indicated in plot 17. The bar at the bottom right of each plot and blue
shading highlight spectra recorded within the first 1 hour.*

320   In contrast, C3-O3 (1059 cm^{-1}) and primary C6-O6 (1034 cm^{-1}) peaks in region ii followed expected
321   trends of decreasing intensities throughout the hydrolysis reaction (Figure 7C). Time resolved spectra in
322   region ii indeed revealed narrow and sharp C3-O3 and primary C6-O6 peaks from the first spectrum at

323   0h, indicating fully hydrated cellulose in this region from the start of the reaction (Figure 8). The C3-O3
324   and primary C6-O6 peaks decreased in intensity over time with minimal changes to the peak shapes. The
325   time courses of the cellulose peaks in region ii thus show that Cel7A action depletes cellulose without
326   appreciably affecting molecular order.

327   ***3.2.2.1   Assessing spatiotemporal changes in molecular order by comparing marker peaks in the***
328   ***cellulose spectra - Lateral Order Index (LOI), Total Crystallinity Index (TCI) and Hydrogen***
329   ***Bonding Index (HBI)***

330   Metrics that have been used to assess changes in cellulose molecular ordering from IR spectra include the
331   lateral order index (LOI), total crystallinity index (TCI), and hydrogen bonding index (HBI). The LOI
332   compares the peak intensity at ~1429 cm^{-1} attributed to δOH of C6-O6H in crystalline regions to the peak
333   intensity at ~896 cm^{-1} associated with amorphous cellulose (56). The TCI compares the peak intensity at
334   1372 cm^{-1} associated with δOH with that of the 2860 cm^{-1} peak due to νCH (57), and the hydrogen
335   bonding index (HBI) compares the ratio of intensities of the peaks at 3345 cm^{-1} νOH due to intra and
336   intermolecular hydrogen bonding (58) and 1337 cm^{-1} due to δOH of O2H and O3H (59). We assessed
337   LOI, TCI and HBI during the first ~5 hours of the reaction where peaks in the hydride-OH region were
338   clearly distinguishable (Figure 6).

339   The algal cellulose used as a substrate in this study was a highly crystalline cellulose with CI ~ 90% (18).
340   Confirming the high degree of crystallinity of algal cellulose, almost no absorbance peak was detected
341   around 896 cm^{-1} such that the LOI values were large (>>1) (Supplemental Information 5). Further, the
342   continued absence of signal at 896 cm^{-1} indicated no increase in amorphous content of the cellulose
343   throughout hydrolysis.

344   The TCI (1372 cm^{-1}/2860 cm^{-1}) hovered around a ratio of ~1.5, with some areas fluctuating between ~ 1
345   and 2 (Figure 9B). Generally tracking the C-O vibration peaks, the intensities of the peaks at 1372 cm^{-1}
346   and 2860 cm^{-1} both decreased over time at similar rates (Figure 9A). At some locations, e.g. at the bottom
347   2/3 of region iii where cellulose depletes at longer times, TCI appear to decrease from ~ 2 to ~0.5-1 over
348   time. Overall, however, the analysis of the TCI indicates minimal impact on total crystallinity by enzyme
349   action, consistent with the expectation that Cel7A, a reducing-end specific cellobiohydrolase acting on
350   accessible productive binding sites at the fibril surfaces, should not significantly alter bulk molecular
351   ordering of cellulose.

352   The HBI (3345 cm^{-1}/1337 cm^{-1}) ranged from ~2 – 20, with an average of ~ 5 (Figure 9D). Both the 3345
353   cm^{-1} and the 1337 cm^{-1} peaks decreased over time (Figure 9C), but depending on the location within
354   regions i and ii, the ratio of the two peaks (HBI) either remained constant or increased with time.
355   Increases in HBI suggests a more rapid loss of cellulose than of hydrogen bonding; i.e. preferential
356   removal of cellulose that is not participating in intermolecular hydrogen bonds. Accessible productive
357   Cel7A binding sites are likely cellulose reducing ends located at microfibril corners and edges that are
358   less extensively hydrogen-bonded within the fibril structures (60). Though the trends are subtle, the HBI
359   suggest that productive Cel7A binding sites are associated with less extensively hydrogen bonded
360   cellulose.

361   Taken together, the three indices, LOI, TCI and HBI, indicated that the algal cellulose is highly ordered,
362   and hydrolysis by Cel7A minimally impacts the overall crystallinity of the cellulose, but preferentially
363   removes less extensively hydrogen bonded cellulose. These trends support previous observations of algal
364   cellulose as a highly crystalline cellulose that erode from the surface due to Cel7A hydrolysis (18), and
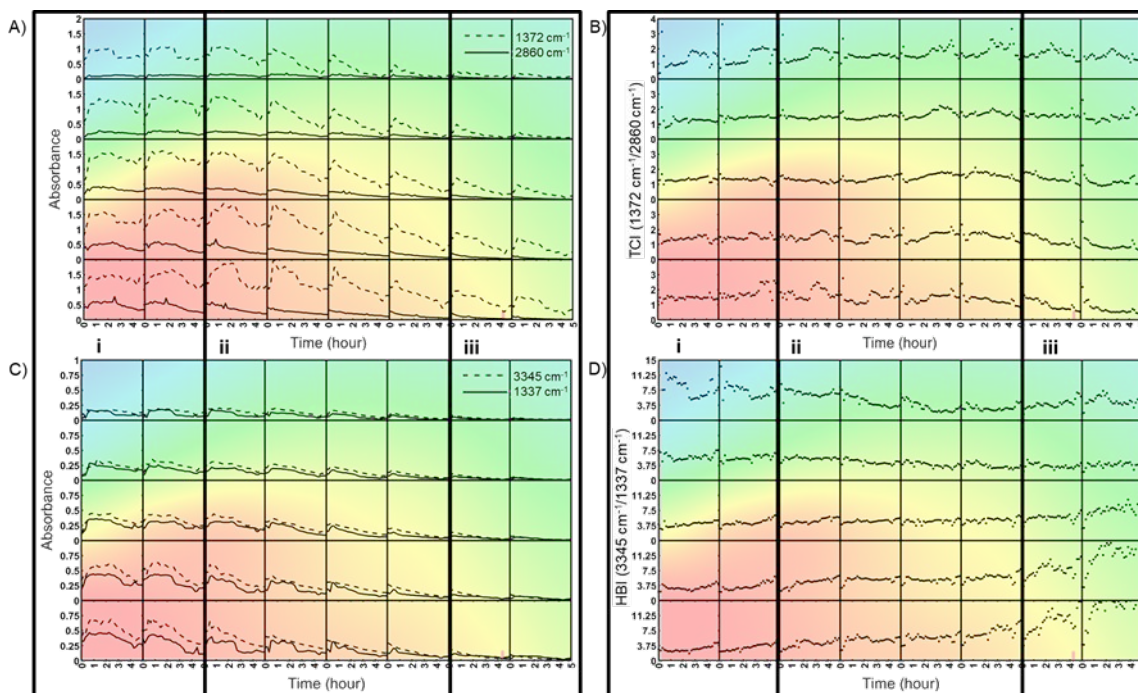365   deplete in accessible productive binding sites during hydrolysis by Cel7A (13).

Figure 9: A) Peak intensities at 1372 cm⁻¹ and 2860 cm⁻¹, and the B) total crystallinity index (TCI) 1372 cm⁻¹/2860 cm⁻¹ over the first 5 hours of enzymatic hydrolysis by Cel7A in regions i, ii, and iii. C) Peak intensities at 3345 cm-1 and 1337 cm-1, and the D) hydrogen bonding index (HBI) 3345 cm⁻¹/1337cm⁻¹ over the first 5 hours of enzymatic hydrolysis by Cel7A in regions i, ii, and iii. The 0-h heat map from (Figure 7A) is overlaid.

366

367   ***3.2.2.2   C6-O6 rotamer ratio as an indicator of molecular order***
368   In highly ordered cellulose I, C6-O6 bonds exist predominantly as *tg* rotamers that hydrogen bond with -
369   O2H2 of the adjacent glucose residue as a hydrogen acceptor (Figure 4). The *gg* rotamer preferentially
370   hydrogen bonds with water, while the *gt* rotamer is favored in air or within non-native cellulose
371   morphologies such as cellulose II and III. In highly ordered cellulose I fibrils, *gg* or *gt* rotamers likely
372   dominate at the aqueous or air interface, and *tg* rotamers would dominate within the fibril (illustrated in
373   Figure 4). The ratio of the C6-O6 rotamers at any location over the course of the enzymatic hydrolysis
374   reaction can provide insights into the impact of Cel7A on molecular ordering of cellulose.

375   The peaks at 1034 cm⁻¹ (primary), 1013 cm⁻¹ (secondary), and 998 cm⁻¹ (minor) are assigned to *tg, gg,* and
376   *gt* rotamers, respectively, based on the analysis of hydrated and dehydrated cellulose above (Section
377   3.1.1). The intensities of the secondary 1013 cm⁻¹, and minor 998 cm⁻¹ peaks generally tracked that of the
378   primary 1034 cm⁻¹ peak during enzymatic hydrolysis (Figure 10A). However, the ratio of the
379   primary:secondary:minor peak intensities (herein referred to as 'C6 ratios') revealed interesting patterns
380   (Figure 10B). For example, there is a noticeable and abrupt change in the temporal trends in the C6 ratios
381   at around 5 hours, coinciding with increased water into the reaction. As discussed above, molecular
382   ordering of cellulose in region i increased due to hydration during the first 5 hours; here, manifesting as
383   increasing C6-ratios in Figure 10B. In region ii, the C6 ratios appeared to decrease during the first 5 hours
384   (Figure 10B). During this time, of the three C6-O6 peaks, the primary peak at 1034 cm⁻¹ exhibited the
385   steepest decrease in intensity, suggesting that an accelerated loss of the *tg* rotamer drove the decreasing
386   C6-O6 ratio (Figure 10A). A more rapid loss of the *tg* rotamer of cellulose is consistent with removing

387 cellulose from the corners of the fibrils. For example, as Cel7A processively hydrolyzes a corner chain of
388 cellulose, it removes both interior C6-O6 groups (likely *tg*) and C6-O6 groups at the aqueous interface
389 (more likely *gg*). This alone would preserve the original C6 ratio; but removing a corner chain exposes
390 C6-O6 of a previously interior chain, converting some *tg* rotamers to *gg*, thereby decreasing the C6 ratio
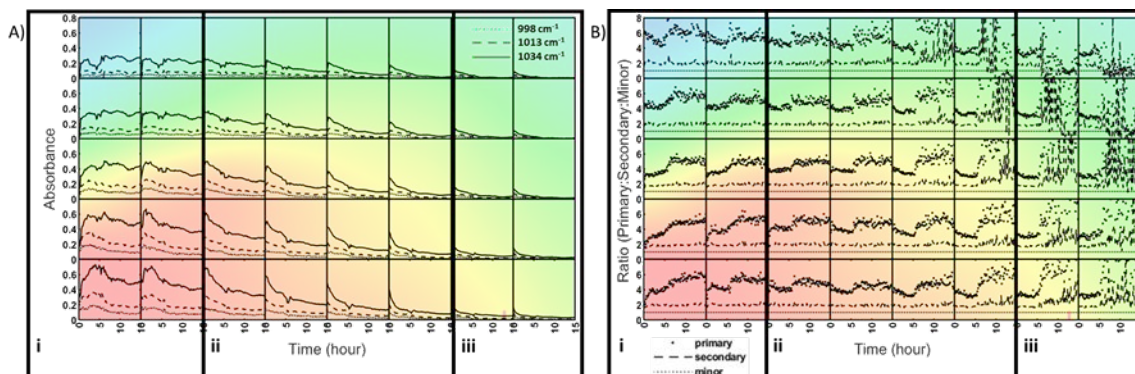391 (asterisks in Figure 4).

Figure 10: A) Peak intensities of the minor (998 cm^{-1}), secondary (1013 cm^{-1}), and primary (2860 cm^{-1}) peaks over 15 hours. B) Ratio of peak intensities of the primary:secondary:minor C6-O6 absorption bands.

392 Within the first 5 hours, C6 ratios decreased to ~ 3:2:1. Just after 5 hours, coinciding with the introduction
393 of excess water into the reaction (Supplemental Material 3), the C6 ratios increased abruptly to ~5:2:1 –
394 ~6:2:1 (Figure 10B). A possible explanation is the removal of surface enzymes (Figure 6B). It is possible
395 that the presence of enzymes causes surface disorder of cellulose, and replacing the enzymes with water
396 restores ordering. Where cellulose is fully depleted due to hydrolysis (e.g. region iii), the excessive scatter
397 in the C6 ratios render them meaningless.

4   Discussion

399 Spatial heterogeneity in the hydrolysis of cellulose by cellulases is posited to contribute strongly to the
400 overall recalcitrance of cellulose (13,61,62), but is challenging to characterize. IR spectromicroscopy
401 enables highly resolved spatial mapping of material composition by bond vibrational modes. In this work,
402 IR spectromicroscopy enabled spatial mapping of changes to cellulose abundance and molecular ordering
403 during enzyme action. The use of a microfluidics system to control temperature, moisture and humidity
404 levels facilitated data collection over 15 hours in an aqueous buffered reaction.

405 Moisture has been a major impediment to IR spectromicroscopy because of strong infrared absorption by
406 water. While water is a critical component of most biological reactions including cellulose hydrolysis,
407 water has also been implicated in imparting changes to molecular ordering of cellulose crystalline fibrils
408 (63,64). The extent of intrafibril hydrogen bonding within cellulose fibrils contribute to the crystalline
409 morphology and crystallinity of cellulose. In this study, spatially resolved changes in localized molecular
410 ordering of cellulose was assessed from examining the key peaks of cellulose in the IR fingerprint region.
411 Glycosidic bonds along the backbone of cellulose are braced on either side by the O5-HO3 and O2H-O6
412 intramolecular hydrogen bonding (Figure 4). The bracing imparts rigidity to the cellulose molecule (65)
413 such that cello-oligosaccharides decrease in solubility with increasing degrees of polymerization (DP),
414 and chains with DP ≥ 6 are insoluble in water (66). Moreover, the O2H-O6 hydrogen bond, occurring on
415 alternating sides of the glycosidic bonds along the molecule, is suggested to strain the molecule and cause
416 the right-handed twist observed in cellulose fibrils (67). Previous studies have reported physical
417 manifestation of the release of stress within the fibrils during enzymatic hydrolysis as spontaneous

418   untwisting and kinking of fibrils (25,68,69). Water-cellulose and cellulose-cellulose hydrogen bonding at
419   the surface of cellulose not only impact ordering of surface chains, but disorder could propagate into the
420   cellulose fibril structure (60,63). Here, we found that cellulose peaks associated with intra- and
421   intermolecular hydrogen bonds in the IR fingerprint region decreased in frequency when dried, implying
422   that these C-O bonds (C2-O2, C3-O3, and C6-O6) are less stiff at the air-cellulose interface than the
423   water-cellulose interface. Furthermore, the ratios of the peak intensities of the three rotameric forms of
424   C6-O6 *tg:gg:gt* shifted from ~ 6:2:1 in ordered cellulose and ~2:1:1 in disordered cellulose. Frequency
425   shifts in the C-O bonds that participate in intra- and intermolecular hydrogen bonding between the wet
426   and dried state are likely due to differences in hydrogen bonding patterns at the water-cellulose and air-
427   cellulose interface. Thus, frequency shifts of the C2-O2, C3-O3, and C6-O6 peaks, and intensity ratios of
428   the C6-O6 rotamers are useful indicators assessing changes to surface ordering of cellulose.

429   The precise role of 'crystallinity' in the resistance of cellulose to hydrolysis has been difficult to
430   elucidate. Most often, the crystallinity index (CI), a bulk measure of the fraction of ordered cellulose in a
431   given sample, is used to query the relationship between crystallinity and cellulose digestibility. However,
432   cellulose CI, including those estimated from peak ratios in the FTIR spectra of cellulose, remains an
433   ambiguous measure of cellulose digestibility (18,28,29). This is not to say that cellulose crystallinity, or
434   molecular ordering of cellulose molecules, particularly at the water-fibril interface is irrelevant to
435   enzymatic hydrolysis. Cellulase hydrolysis of cellulose is an interfacial reaction where cellulases must
436   decrystallize and complex to isolated cellulose molecules at the surface of the fibrils. Or, cellulases must
437   locate a decrystallized cellulose molecule at the surface of the fibrils to complex with. Thus, a reasonable
438   hypothesis is that localized surface disorder in molecular arrangement offers more productive binding
439   sites (70). The algal cellulose used in this study was a highly crystalline and recalcitrant cellulose. In our
440   previous studies, we showed that Cel7A is insensitive to the number of reducing ends (or degree of
441   polymerization) and total crystallinity of algal cellulose (18); however, initial cellulose hydrolysis rates by
442   Cel7A correlates with initial binding capacity of cellulose (10), and Cel7A rapidly depletes available
443   productive binding sites on the cellulose, leaving a substrate that is essentially impenetrable to the
444   cellobiohydrolase (13). Indeed, spatial mapping of FTIR spectra in this study showed that the algal
445   cellulose was not uniformly resistant to Cel7A hydrolysis. Some regions appeared to be completely
446   hydrolyzed by Cel7A while others did not appear to deplete significantly.

447   An unanswered question from this study is whether cellulase action creates localized disorder at the
448   cellulose surface? Or, does localized disorder at cellulose surfaces invite active cellulase complexation? A
449   more detailed study with higher spatial resolution is necessary to adequately query these questions, to
450   help inform future efforts in enzyme engineering to improve enzyme's ability to decrystallize and
451   complex to cellulose, and biomass pretreatment strategies targeting desired cellulose surface properties.

452   **5   Conclusions**

453   In-situ, spatial mapping of the infrared spectra of cellulose during enzymatic hydrolysis in buffer was
454   successfully achieved using an open-channel humidity-controlled microfluidics device. The spatial
455   heterogeneity in hydrolysis rates and changes in molecular ordering of cellulose over the course of
456   hydrolysis by Cel7A was documented. To our knowledge, this is the first documented in situ study of
457   spatiotemporal changes in cellulose during enzymatic hydrolysis in buffer by IR spectral mapping. A
458   major advantage of in situ measurements is tracking of both peak amplitudes and peak centers, to assess
459   depletion rates and changes in molecular ordering of cellulose.

460   Here, we established a label-free, spatial and time-resolved infrared spectroscopic method towards filling
461   the knowledge-gap of how cellulose supramolecular ordering contributes to hydrolysis mechanism and

462   ultimately hydrolysis kinetics. The insights gained with work on isolated cellulose paves the way for
463   future analyses of cellulose within plant cell wall matrices (i.e. lignocellulosic biomass), towards fulfilling
464   the vision for low-cost bioconversion of lignocellulosic materials to sustainable fuels, chemicals and
465   materials.

6   Author Contributions

467   Tina Jeoh: Conceptualization, validation, investigation, resources, writing – review & editing,
468   visualization, supervision, project administration, funding acquisition

469   Jennifer Danger Nill: Conceptualization, validation, investigation, methodology, formal analysis,
470   visualization, writing – review & editing

471   Wujun Zhao: Investigation, methodology

472   Sankar Raju Narayanasamy: Investigation, methodology, visualization, writing – review & editing

473   Liang Chen: methodology, formal analysis, visualization

474   Hoi-Ying Holman: Conceptualization, validation, investigation, resources, writing – review & editing,
475   visualization, supervision, project administration, funding acquisition

7   Acknowledgements

8   Supplemental Materials

486   SM1 Cellulose spectra and peak assignments

487   SM2 Cellulose dehydration

488   SM3 Water levels during enzymatic hydrolysis

489   SM4 IR peak intensities over time

490   SM5 LOI and HBI

491   Raw spectral data are published and available via the Dryad database (doi:10.25338/B8NP9P)

9   References

493   1.   Field JL, Richard TL, Smithwick EAH, Cai H, Laser MS, LeBauer DS, et al. Robust paths to net
494   greenhouse gas mitigation and negative emissions via advanced biofuels. Proc Natl Acad Sci USA.
495   2020 Sep 8;117(36):21968.

496   2.   Scarlat N, Dallemand JF. Chapter Ten - Future Role of Bioenergy. In: Lago C, Caldés N, Lechón Y,
497   editors. The Role of Bioenergy in the Bioeconomy: Resources, Technologies, Sustainability and

498   Policy [Internet]. Academic Press; 2019. p. 435–547. Available from:
499   https://www.sciencedirect.com/science/article/pii/B9780128130568000108

500 3. Klemm D, Cranston ED, Fischer D, Gama M, Kedzior SA, Kralisch D, et al. Nanocellulose as a
501   natural source for groundbreaking applications in materials science: Today's state. Materials Today.
502   2018 Sep;21(7):720–48.

503 4. Mokhena TC, John MJ. Cellulose nanomaterials: new generation materials for solving global issues.
504   Cellulose. 2020 Feb;27(3):1149–94.

505 5. Yang X, Reid MS, Olsén P, Berglund LA. Eco-Friendly Cellulose Nanofibrils Designed by Nature:
506   Effects from Preserving Native State. ACS Nano. 2020 Jan 28;14(1):724–35.

507 6. Filson PB, Dawson-Andoh BE, Schwegler-Berry D. Enzymatic-mediated production of cellulose
508   nanocrystals from recycled pulp. Green Chem. 2009;11(11):1808.

509 7. Pirich CL, Picheth GF, Fontes AM, Delgado-Aguilar M, Ramos LP. Disruptive enzyme-based
510   strategies to isolate nanocelluloses: a review. Cellulose. 2020 Jul;27(10):5457–75.

511 8. Moreau C, Tapin-Lingua S, Grisel S, Gimbert I, Le Gall S, Meyer V, et al. Lytic polysaccharide
512   monooxygenases (LPMOs) facilitate cellulose nanofibrils production. Biotechnol Biofuels. 2019
513   Dec;12(1):156.

514 9. Jalak J, Väljamäe P. Multi-Mode Binding of Cellobiohydrolase Cel7A from *Trichoderma reesei* to
515   Cellulose. PLoS ONE. 2014;9(9):e108181.

516 10. Karuna N, Jeoh T. The productive cellulase binding capacity of cellulosic substrates. Biotechnology
517   and Bioengineering. 2017;114(3):533–42.

518 11. Cruys-Bagger N, Alasepp K, Andersen M, Ottesen J, Borch K, Westh P. Rate of Threading a
519   Cellulose Chain into the Binding Tunnel of a Cellulase. The journal of physical chemistry B. 2016
520   Jun 30;120(25):5591–600.

521 12. Nill J, Karuna N, Jeoh T. The impact of kinetic parameters on cellulose hydrolysis rates. Process
522   Biochemistry. 2018 Nov 1;74:108–17.

523 13. Nill JD, Jeoh T. The Role of Evolving Interfacial Substrate Properties on Heterogeneous Cellulose
524   Hydrolysis Kinetics. ACS Sustainable Chem Eng. 2020 May 4;8(17):6722–33.

525 14. Horikawa Y, Konakahara N, Imai T, Kentaro A, Kobayashi Y, Sugiyama J. The structural changes in
526   crystalline cellulose and effects on enzymatic digestibility. Polymer Degradation and Stability. 2013
527   Nov 1;98(11):2351–6.

528 15. Bansal P, Vowell BJ, Hall M, Realff MJ, Lee JH, Bommarius AS. Elucidation of cellulose
529   accessibility, hydrolysability and reactivity as the major limitations in the enzymatic hydrolysis of
530   cellulose. Bioresource Technology. 2012 Mar 1;107:243–50.

531 16. Jeoh T, Ishizawa C, Davis MF, Himmel ME, Adney WS, Johnson DK. Cellulase Digestibility of
532   Pretreated Biomass is Limited by Cellulose Accessibility. Biotechnology and bioengineering.
533   2007;98(1):112–22.

534   17. Jeoh T, Cardona MJ, Karuna N, Mudinoor AR, Nill J. Mechanistic kinetic models of enzymatic
535   cellulose hydrolysis—A review. Biotechnology and Bioengineering. 2017 Jul 1;114(7):1369–85.

536   18. O'Dell PJ, Mudinoor AR, Parikh SJ, Jeoh T. The Effect of Fibril Length and Architecture on the
537   Accessibility of Reducing Ends of Cellulose Iα to *Trichoderma reesei* Cel7A. Cellulose.
538   2015;22(3):1697–713.

539   19. Arantes V, Saddler JN. Cellulose accessibility limits the effectiveness of minimum cellulase loading
540   on the efficient hydrolysis of pretreated lignocellulosic substrates. Biotechnology for biofuels.
541   2011;4(1):3.

542   20. Väljamäe P, Sild V, Pettersson G, Johansson G. The initial kinetics of hydrolysis by
543   cellobiohydrolases I and II is consistent with a cellulose surface− erosion model. European Journal of
544   Biochemistry. 1998;253(2):469–75.

545   21. Santa-Maria M, Jeoh T. Molecular-scale investigations of cellulose microstructure during enzymatic
546   hydrolysis. Biomacromolecules. 2010;11(8):2000–7.

547   22. Igarashi K, Koivula A, Wada M, Kimura S, Penttilä M, Samejima M. High Speed Atomic Force
548   Microscopy Visualizes Processive Movement of Trichoderma reesei Cellobiohydrolase I on
549   Crystalline Cellulose. J Biol Chem. 2009 Dec 25;284(52):36186–90.

550   23. Eibinger M, Bubner P, Ganner T, Plank H, Nidetzky B. Surface structural dynamics of enzymatic
551   cellulose degradation, revealed by combined kinetic and atomic force microscopy studies. Febs
552   Journal. 2014;281(1):275–90.

553   24. Jung J, Sethi A, Gaiotto T, Han JJ, Jeoh T, Gnanakaran S, et al. Binding and movement of individual
554   Cel7A cellobiohydrolases on crystalline cellulose surfaces revealed by single-molecule fluorescence
555   imaging. J Biol Chem. 2013 Jul 1;288(33):24164–72.

556   25. Mudinoor AR, Goodwin PM, Rao RU, Karuna N, Hitomi A, Nill J, et al. Interfacial molecular
557   interactions of cellobiohydrolase Cel7A and its variants on cellulose. Biotechnol Biofuels. 2020
558   Dec;13(1):10.

559   26. Ding SY, Liu YS, Zeng Y, Himmel ME, Baker JO, Bayer EA. How Does Plant Cell Wall Nanoscale
560   Architecture Correlate with Enzymatic Digestibility? Science. 2012 Nov 23;338(6110):1055–60.

561   27. Holman HYN, Miles R, Hao Z, Wozei E, Anderson LM, Yang H. Real-Time Chemical Imaging of
562   Bacterial Activity in Biofilms Using Open-Channel Microfluidics and Synchrotron FTIR
563   Spectromicroscopy. Anal Chem. 2009 Oct 15;81(20):8564–70.

564   28. Corgié SC, Smith HM, Walker LP. Enzymatic transformations of cellulose assessed by quantitative
565   high-throughput fourier transform infrared spectroscopy (QHT-FTIR). Biotechnol Bioeng. 2011
566   Jul;108(7):1509–20.

567   29. Kruer-Zerhusen N, Cantero-Tubilla B, Wilson DB. Characterization of cellulose crystallinity after
568   enzymatic treatment using Fourier transform infrared spectroscopy (FTIR). Cellulose. 2018
569   Jan;25(1):37–48.

570   30. Cao Y, Tan HM. Effects of cellulase on the modification of cellulose. Carbohyd Res. 2002
571   Aug;337(14):1291–6.

572   31. Sills DL, Gossett JM. Using FTIR to predict saccharification from enzymatic hydrolysis of alkali-
573   pretreated biomasses. Biotechnol Bioeng. 2012 Feb;109(2):353–62.

574   32. Spiridon I, Teacă CA, Bodîrlău R. Structural changes evidenced by FTIR spectroscopy in cellulosic
575   materials after pre-treatment with ionic liquid and enzymatic hydrolysis. BioRes. 2010 Dec
576   20;6(1):400–13.

577   33. Devaux MF, Jamme F, André W, Bouchet B, Alvarado C, Durand S, et al. Synchrotron Time-Lapse
578   Imaging of Lignocellulosic Biomass Hydrolysis: Tracking Enzyme Localization by Protein
579   Autofluorescence and Biochemical Modification of Cell Walls by Microfluidic Infrared
580   Microspectroscopy. Front Plant Sci. 2018 Feb 20;9:200–200.

581   34. Loutherback K, Birarda G, Chen L, Holman HYN. Microfluidic Approaches to Synchrotron
582   Radiation-Based Fourier Transform Infrared (SR-FTIR) Spectral Microscopy of Living Biosystems.
583   Protein and Peptide Letters. 2016 received;23(3):273–82.

584   35. Gierlinger N, Goswami L, Schmidt M, Burgert I, Coutand C, Rogge T, et al. In situ FT-IR
585   microscopic study on enzymatic treatment of poplar wood cross-sections. Biomacromolecules. 2008
586   Aug;9(8):2194–201.

587   36. Holman HY, Zhao W, Narayanasamy SR. Devices and Methods for Diagnostic Spectroscopy of
588   Biomaterials and Live Cells. WO2022226148A1.

589   37. Holman HY, Zhao W, Nill J, Chen L, Narayanasamy SR, Jeoh T. An open-channel microfluidic
590   membrane device for in situ hyperspectral mapping of enzymatic cellulose hydrolysis. 2021.

591   38. Zhao W, Holman HY, Jeoh T. Time and Spatially-Resolved Fourier-Transform Infrared (FTIR)
592   Spectromicroscopy of Cellulose in Buffered Reactions with Trichoderma reesei Cel7A. Dryad; 2023.

593   39. Hofstetter K, Hinterstoisser B, Salmén L. Moisture uptake in native cellulose – the roles of different
594   hydrogen bonds: a dynamic FT-IR study using Deuterium exchange. Cellulose. 2006 Apr;13(2):131–
595   45.

596   40. Olsson AM, Salmén L. The association of water to cellulose and hemicellulose in paper examined by
597   FTIR spectroscopy. Carbohydrate Research. 2004 Mar;339(4):813–8.

598   41. Nishiyama Y, Chanzy H, Langan P. Synchrotron and X-ray Neutron Fiber Diffraction Studies of
599   Cellulose Polymorphs. Polymer Preprints. 2001;42(2).

600   42. Nishiyama Y, Chanzy H, Wada M, Sugiyama J, Mazeau K, Forsyth VT, et al. Synchrotron and X-ray
601   Neutron Fiber Diffraction Studies of Cellulose Polymorphs. In: Advances in X-ray Analysis. 2002. p.
602   385.

603   43. Cael JJ, Gardner KH, Koenig JL, Blackwell J. Infrared and Raman spectroscopy of carbohydrates.
604   Paper V. Normal coordinate analysis of cellulose I. The Journal of Chemical Physics. 1975 Feb
605   1;62(3):1145–53.

606   44. Marchessault RH, Sundararajan PR. Chapter 2 - Cellulose. In: Aspinall GO, editor. The
607   Polysaccharides [Internet]. Academic Press; 1983. p. 11–95. Available from:
608   https://www.sciencedirect.com/science/article/pii/B9780120656028500078

609   45. McCann MC, Stacey NJ, Wilson R, Roberts K. Orientation of macromolecules in the walls of
610   elongating carrot cells. Journal of Cell Science. 1993 Dec 1;106(4):1347–56.

611   46. Chen L, Wilson RH, McCann MC. Infra-red microspectroscopy of hydrated biological systems:
612   design and construction of a new cell with atmospheric control for the study of plant cell walls.
613   Journal of Microscopy. 1997 Oct 1;188(1):62–71.

614   47. Makarem M, Lee CM, Kafle K, Huang S, Chae I, Yang H, et al. Probing cellulose structures with
615   vibrational spectroscopy. Cellulose. 2019 Jan 1;26(1):35–79.

616   48. Wilson RH, Smith AC, Kačuráková M, Saunders PK, Wellner N, Waldron KW. The Mechanical
617   Properties and Molecular Dynamics of Plant Cell Wall Polysaccharides Studied by Fourier-
618   Transform Infrared Spectroscopy1. Plant Physiology. 2000 Sep 1;124(1):397–406.

619   49. Nishiyama Y. Structure and properties of the cellulose microfibril. Journal of Wood Science. 2009
620   Aug;55(4):241–9.

621   50. Newman RH, Davidson TC. Molecular conformations at the cellulose–water interface. Cellulose.
622   2004 Mar;11(1):23–32.

623   51. Viëtor RJ, Newman RH, Ha MA, Apperley DC, Jarvis MC. Conformational features of crystal-
624   surface cellulose from higher plants. The Plant Journal. 2002 Jun 1;30(6):721–31.

625   52. Park S, Johnson DK, Ishizawa CI, Parilla PA, Davis MF. Measuring the Crystallinity Index of
626   Cellulose by Solid State ^{13}C Nuclear Magnetic Resonance. Cellulose. 2009;16(4):641–7.

627   53. Olsen JP, Donohoe BS, Borch K, Westh P, Resch MG. Interrelationships between cellulase activity
628   and cellulose particle morphology. Cellulose. 2016 Aug 1;23(4):2349–61.

629   54. Schwanninger M, Rodrigues JC, Pereira H, Hinterstoisser B. Effects of short-time vibratory ball
630   milling on the shape of FT-IR spectra of wood and cellulose. Vibrational Spectroscopy. 2004
631   Oct;36(1):23–40.

632   55. Kotov N, Larsson PA, Jain K, Abitbol T, Cernescu A, Wågberg L, et al. Elucidating the fine-scale
633   structural morphology of nanocellulose by nano infrared spectroscopy. Carbohydrate Polymers. 2023
634   Feb;302:120320.

635   56. Nada AMA, Mohamed SH, Abd El Mongy S, Seoudi R. Preparation, vibrational structure and
636   dielectric properties studies of cotton linter and its derivatives. Journal of Non-Crystalline Solids.
637   2009 Dec;355(52–54):2544–9.

638   57. Nelson ML, O'Connor RT. Relation of certain infrared bands to cellulose crystallinity and crystal
639   lattice type. Part II. A new infrared ratio for estimation of crystallinity in celluloses I and II. J Appl
640   Polym Sci. 1964 May;8(3):1325–41.

641   58. Lee CM, Kubicki JD, Fan B, Zhong L, Jarvis MC, Kim SH. Hydrogen-Bonding Network and OH
642   Stretch Vibration of Cellulose: Comparison of Computational Modeling with Polarized IR and SFG
643   Spectra. J Phys Chem B. 2015 Dec 10;119(49):15138–49.

644   59. Marechal Y, Chanzy H. The hydrogen bond network in Ib cellulose as observed by infrared
645   spectrometry. Journal of Molecular Structure. 2000;14.

646 60. Beckham GT, Matthews JF, Peters B, Bomble YJ, Himmel ME, Crowley MF. Molecular-Level
647   Origins of Biomass Recalcitrance: Decrystallization Free Energies for Four Common Cellulose
648   Polymorphs. J Phys Chem B. 2011 Apr;115(14):4118–27.

649 61. Jalak J, Valjamae P. Mechanism of Initial Rapid Rate Retardation in Cellobiohydrolase Catalyzed
650   Cellulose Hydrolysis. Biotechnol Bioeng. 2010 Aug;106(6):871–83.

651 62. Kurasin M, Valjamae P. Processivity of Cellobiohydrolases Is Limited by the Substrate. J Biol Chem.
652   2011 Jan;286(1):169–77.

653 63. Matthews JF, Skopec CE, Mason PE, Zuccato P, Torget RW, Sugiyama J, et al. Computer simulation
654   studies of microcrystalline cellulose I beta. Carbohyd Res. 2006 Jan;341(1):138–52.

655 64. Maurer RJ, Sax AF, Ribitsch V. Molecular simulation of surface reorganization and wetting in
656   crystalline cellulose I and II. Cellulose. 2013 Feb;20(1):25–42.

657 65. Qian XH. The effect of cooperativity on hydrogen bonding interactions in native cellulose I beta from
658   ab initio molecular dynamics simulations. Molecular Simulation. 2008;34(2):183–91.

659 66. Taylor JB. The Water Solubilities and Heats of Solution of Short Chain Cellulosic Oligosaccharides.
660   Transactions of the Faraday Society. 1957;53(9):1198–203.

661 67. Bu L, Himmel ME, Crowley MF. The molecular origins of twist in cellulose I-beta. Carbohydrate
662   Polymers. 2015 10;125:146–52.

663 68. Bowling AJ, Amano Y, Lindstrom R, Brown MBJ. Rotation of Cellulose Ribbons During
664   Degradation with Fungal Cellulase. Cellulose. 2001;8:91–7.

665 69. Ciesielski PN, Wagner R, Bharadwaj VS, Killgore J, Mittal A, Beckham GT, et al. Nanomechanics
666   of cellulose deformation reveal molecular defects that facilitate natural deconstruction. Proc Natl
667   Acad Sci USA. 2019 Apr 29;201900161.

668 70. Uchiyama T, Uchihashi T, Ishida T, Nakamura A, Vermaas JV, Crowley MF, et al. Lytic
669   polysaccharide monooxygenase increases cellobiohydrolases activity by promoting decrystallization
670   of cellulose surface. Sci Adv. 2022 Dec 23;8(51):eade5155.

671

672